Simulation Analysis of Obstacle Crossing Stability for Transmission Line Inspection Robot

Qianli Wang

School of Mathematics and Computer Science, Yichun University, Yichun, 336000, China

Abstract—As an indispensable energy source in production and daily life, electricity has important implications in the operation of society and economic development. As the hub of power transmission, the safety of transmission lines is related to the stability of the power grid. Regular inspection of transmission lines is an effective measure to ensure the stability of the power system. Patrol robots are used for regular inspection of transmission lines due to their advantages such as low cost and long running time. To achieve collision free, the study proposes an obstacle path planning algorithm based on an improved bidirectional fast expanding random tree through kinematic analysis of the robot. According to the experimental results, when overtaking the damper, the rotation ranges of the 1st claw/arm and the 2nd bracket/arm/claw were (0°~22°), (-50°, 10°), (0°, 25°), (-50°, 10°), and (0°, 22°), respectively. The corresponding rotational speeds were (-1.5~1.5) deg/s, (-3, 2.5) deg/s, (-3.5~3.5) deg/s, (-2.5, 3) deg/s, and (-27, 2) deg/s, respectively. The expansion and contraction ranges of the upper, middle, lower, and horizontal push rods were (0, 100) mm, (0, 110) mm, (-60, 10) mm, and (0, 20) mm, respectively. From the above results, when crossing obstacles, the motion acceleration of the inspection robot is not significant. The speed changes smoothly. The obstacle crossing path planning algorithm proposed in the study can achieve stable motion of the inspection robot.

Keywords—*Transmission line; inspection robot; obstacle crossing path; kinematic analysis; bidirectional fast expanding random tree*

I. INTRODUCTION

To meet daily production and living needs, power plants transmit electricity to various regions through high-voltage transmission lines. Due to long-term exposure of high-voltage transmission lines to the wild, various faults continue to occur, posing a threat to the safety of the power grid. Meanwhile, with the continuous growth of electricity demand, the mileage of high-voltage transmission lines has also rapidly increased. A large number of high-voltage transmission lines penetrate into areas that are rarely visited, posing great difficulties for circuit inspection work. This makes it difficult to detect transmission line faults in a timely manner, increasing the probability of safety accidents occurring [1-2]. Compared with manual inspections and drone inspections, inspection robots have high inspection quality, low cost, and long working hours, making them suitable for various environments. In addition to cables, there are also various metal fittings on the transmission line, which are obstacles for inspection robots. Therefore, to ensure the inspection range, the inspection robot needs to cross these obstacles [3-4]. In recent years, with the vigorous development of various technologies such as machine vision, deep learning,

intelligent sensors, and intelligent Internet of Things, overhead transmission line inspection robots have also ushered in new development opportunities. For example, combining machine vision, deep learning, and multi-sensor information fusion technologies can achieve online obstacle recognition, localization, and model construction. Based on obstacle models, online obstacle crossing path planning can be performed to ensure that the patrol robot has obstacle crossing capabilities in different obstacle and attitude environments. It can also be combined with intelligent IoT technology to achieve real-time feedback monitoring and adjustment of the entire obstacle crossing process. Therefore, the research on obstacle crossing path planning for overhead transmission line patrol robots in this article has great practical application significance. In the current field of 110kV overhead transmission line inspection robots, the main obstacle crossing technology solutions include linear guide rail and linkage robotic arm. However, each has its own advantages and disadvantages. The former is stable and reliable when crossing obstacles, but the overall weight is too large, the load capacity is low, and the obstacle crossing distance is short. The latter has lower overall weight and improved obstacle crossing distance, but requires higher requirements for rotary joint motors and lower reliability in obstacle crossing. Meanwhile, due to the complexity of obstacle crossing actions, it is difficult to ensure that the relative position and posture of the line patrol robot and obstacles are fixed during each obstacle crossing operation. Pre-planning and fixing the obstacle crossing action sequence for each obstacle can easily lead to collisions with obstacles, wires, etc. during the obstacle crossing process, resulting in failure. Therefore, to improve the work efficiency of Transmission Line Inspection Robot (TLIR) and achieve collision free motion of inspection robots, a cost-effective obstacle crossing path planning method for inspection robots based on the improved Rapidly Expanding Random Tree-Connect (RRT-Connect) is proposed. By improving joint motion and search step size, and setting an intermediate random tree, the RRT-Connect algorithm being prone to local search is improved, simplifying the search process.

Rest of the study is divided into five sections. Section II will briefly describe the research status of transmission line inspection robots and RRT algorithms. Section III will conduct dynamic analysis on the optional robot and designs the obstacle crossing path planning algorithm. Section IV will simulate and analyze the obstacle crossing performance of the inspection robot. Section V will discuss the research results to further analyze them. Section VI will summarize the research of the entire article.

II. RELATED WORKS

With the increasing demand for transmission lines in the power system, it has become a current trend for inspection robots to conduct line inspections. Wang et al. [5] proposed a new four arm inspection robot to address the low obstacle crossing efficiency and poor safety of inspection robots. This new inspection robot had a rectangular frame on its walking arm to improve obstacle crossing efficiency. In addition, the robot could also use two different sets of arms to cross the tension tower together. The experimental results showed that the new four arm inspection robot could cross common obstacles on transmission lines. Wei et al. [6] proposed a lateral friction recognition method based on fuzzy control to address the limited movement of inspection robots. This method monitored the friction between the walking wheel line and the wheel flange, effectively avoiding "wheel line" jamming caused by external uncertain factors. This method could effectively improve the automation and intelligence level of the operation and transmission system of the inspection robot. Huang et al. [7] proposed a detection method based on visual sensors for rapid detection of wire looseness issues. This method collected wire images through an image acquisition system. The GEG algorithm was used for foreground highlighting and hierarchical enhancement. The implementation results showed that this method could quickly detect loose wires. Qingkai et al. [8] proposed a fault detection method based on lightweight semantic segmentation network to address the accuracy in line fault detection. A two branch network was designed to locate instances and refine contours. This method improved the accuracy of line fault detection. Xiong et al. [9] proposed an object recognition model based on human concept learning to address the automatic fault detection for inspection robots. The model was preliminarily identified through Mask R-CNN. Bayesian contextual network was used for result correction. Compared with other methods, the accuracy of this method was increased by 9.7%.

As a tree-based algorithm, RRT is suitable for multi-dimensional space, with simple principles and strong applicability. It is a typical path planning algorithm. Hu B et al. [10] proposed a path planning algorithm based on RRT to find accessible paths for wheeled robots. This algorithm used a motion control law guided by a posture-based steering function to reach its destination. From the experimental results, the trajectory generated by this method was smoother and shorter in length. Sun et al. [11] proposed a motion planning method based on the SC-RRT algorithm for autonomous navigation of mobile robots. This method improved the branch growth mode of the RRT-Connect algorithm, reduced the sampling space, and quickly obtained a path away from obstacles. Jhang et al. [12] proposed a motion planning method based on bidirectional fast exploration random trees and Reeds-Shepp curves for the path planning problem of autonomous parking. This method could be independently proposed in complex parking lots. Zammit and Kampen [13] proposed a path planning algorithm based on RRT for real-time safe navigation of unmanned aerial vehicles. From the experimental results, in simple location environments, the RRT algorithm had a success rate of over 95%. Compared with other algorithms, the path was shorter. Wang et al. [14] proposed a hybrid bidirectional fast exploration random tree based on reinforcement learning to address the randomness and slow convergence speed in path generation. This method improved search efficiency and shortened the generation path.

In summary, the research on TLIR has been quite effective. However, most studies overlook the stability of the obstacle crossing process. The RRT algorithm, as a typical path planning algorithm, although suitable for multi-dimensional spaces, is prone to falling into local search. Therefore, to ensure the motion stability of the inspection robot, an obstacle crossing path planning algorithm based on the improved RRT-Connect algorithm is proposed. By improving joint motion and search step size, and setting an intermediate random tree, the traditional RRT-Connect is improved.

III. OBSTACLE CROSSING STABILITY ANALYSIS OF TLIR

In transmission lines, in addition to equipment such as tension towers and cables, it also includes hardware such as insulator strings and spacer rods. These hardware tools that exist in transmission lines are obstacles for TLIR. During the inspection process, whether the robot can stably cross various obstacles is the key to complete the inspection work.

A. Dynamic Analysis of Obstacle Crossing Motion of TLIR

During the obstacle crossing process of the TLIR, one claw of the robot grasps the line and the other claw disengages. The motion of the detachment claw is similar to the reverse motion of the gripping claw. To analyze the obstacle crossing engineering of robots, a kinematic analysis is conducted on the obstacle crossing process of the inspection robot using the D-H parameter method with a horizontal plane as the reference plane. The joint change matrix of the inspection robot is shown in Eq. (1).

$$
{}^{i-1}_{i}T = \begin{bmatrix} \cos\theta_i & -\sin\theta_i\cos\alpha_i & \sin\theta_i\sin\alpha_i & a_i\cos\theta_i \\ \sin\theta & \cos\theta_i\cos\alpha_i & -\cos\theta_i\sin\alpha_i & a_i\sin\theta_i \\ 0 & \sin\alpha_i & \cos\alpha_i & d_i \\ 0 & 0 & 0 & 1 \end{bmatrix} \quad (1)
$$

In Eq. (1), θ_i represents the amount of rotation of the rotating joint, (rad). d_i represents the extension and retraction of the arm, (mm). α_i and a_i are constants. In the link model of the TLIR, the angle relationship between the upper push rod, middle push rod, and wheel claw is shown in Fig. 1.
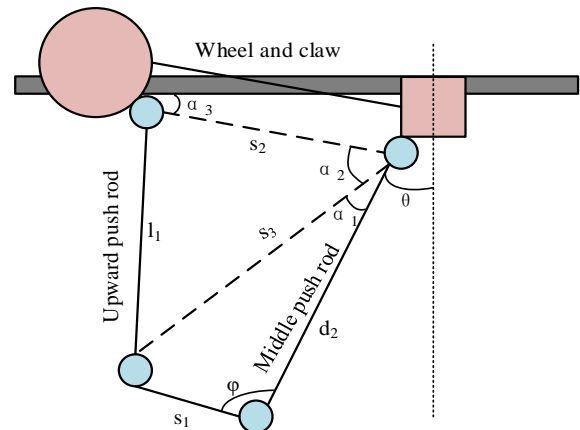

Fig. 1. Upper bar / middle bar and wheel claw angle relationship.

In Fig. 1, the upper push rod is responsible for adjusting the angle between the middle push rod and the wheel claw. According to the relationship shown in the above figure, the geometric relationship among the three is shown in Eq. (2).

$$\begin{cases} s_3 = \sqrt{s_1^2 + d_2^2 - 2s_1 d_2 c \cos\varphi} \\ \alpha_1 = \arccos\left(\dfrac{s_3^2 + d_2^2 - s_1^2}{2s_3 d_2}\right) \\ \alpha_2 = \arccos\left(\dfrac{s_3^2 + s_2^2 - l_1^2}{2s_3 s_2}\right) \\ \theta = \pi - \left(\dfrac{\pi}{2} - \alpha_3\right) - (\alpha_1 + \alpha_2) \end{cases} \quad (2)$$

In Eq. (2), s_3 represents the distance between joint 1 and joint 2. s_1 stands for the length of the connector. d_2 stands for the length of the middle push rod. φ stands for the angle between the middle push rod and the connecting piece. α_1 signifies the angle between s_3 and the middle push rod. α_2 stands for the angle between the wheel claw and s_3. l_1 represents the length of the upper push rod. θ refers to the angle between the middle push rod and the vertical line. α_3 represents the angle between the wheel claw and the horizontal line. According to the length of the middle push rod, the range of the angle between the upper push rod and the wheel claw can be determined. The angle relationship between the lower/middle push rod and the center turntable is illustrated in Fig. 2.
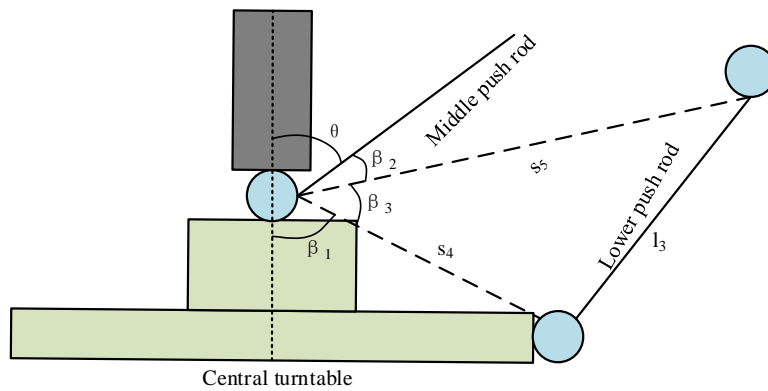

Fig. 2. Angle relationship between lower / middle push rod and center turntable.
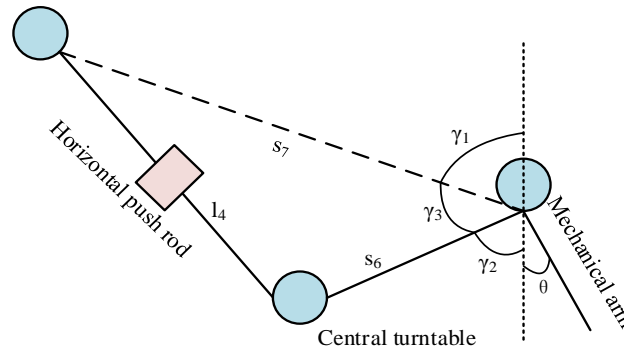

Fig. 3. Angle relationship between horizontal lever / robotic arm and center turntable.

In Fig. 2, the angle between the middle push rod and the center turntable is adjusted by the lower push rod. According to the relationship shown in Fig. 2, the geometric relationship among the three is shown in Eq. (3).

$$\begin{cases} \beta_2 = \arccos\left(\dfrac{s_4^2 + s_5^2 - l_3^2}{2s_4 s_5}\right) \\ \theta = \beta_1 + \beta_2 + \beta_3 - \pi \end{cases} \quad (3)$$

In Eq. (3), β_3 represents the angle between the center turntable and s_5. s_4 represents the length of the central

turntable. s_5 represents the distance between joint 5 and the upper endpoint of the central turntable. l_3 refers to the length of the lower push rod. β_1 refers to the angle between the center turntable and the vertical line. β_2 is the angle between the middle push rod and s_5. The relationship between the horizontal push rod/robotic arm and the center turntable angle is shown in Fig. 3.

In Fig. 3, the angle between the robotic arm and the central turntable is adjusted by a horizontal push rod. According to the relationship shown in the above figure, the geometric relationship expression among the three is shown in Eq. (4).

$$\begin{cases} \gamma_3 = \arccos\left(\dfrac{s_6^2 + s_7^2 - l_4^2}{2 s_6 s_7}\right) \\ \theta' = \gamma_1 + \gamma_2 + \gamma_3 - \pi \end{cases} \quad (4)$$

In Eq. (4), γ_3 represents the angle between s_7 and the central turntable. s_6 represents the length of the central turntable. l_4 refers to the length of the horizontal push rod. θ' refers to the angle between the robotic arm and the vertical line. γ_1 refers to the angle between s_7 and the vertical line. γ_2 refers to the angle between the center turntable and the vertical line. The D-H parameters of each connecting rod can be combined with Eq. (1) to obtain the homogeneous transformation matrix of each joint. Directly below the transmission line is the origin of the global coordinate system. The homogeneous transformation matrix of the inspection robot end in the global coordinate system can be obtained by multiplying the Homogeneous Transformation Matrices (HTM) between different coordinate systems, as displayed in Eq. (5).

$$_{7}^{G}T = _{0}^{G}T \cdot _{1}^{0}T \cdot _{2}^{1}T \cdot _{3}^{2}T \cdot _{4}^{3}T \cdot _{5}^{4}T \cdot _{6}^{5}T \cdot _{7}^{6}T = \begin{bmatrix} n_x & o_x & a_x & p_x \\ n_y & o_y & a_y & p_y \\ n_z & o_z & a_z & p_z \\ 0 & 0 & 0 & 1 \end{bmatrix} \quad (5)$$

In Eq. (5), $_{7}^{G}T$ stands for the HTM of coordinate system 7 relative to the global coordinate system. $_{0}^{G}T$ stands for the HTM of coordinate system 0 relative to the global coordinate system. $_{1}^{0}T$, $_{2}^{1}T$, $_{3}^{2}T$, $_{4}^{3}T$, $_{5}^{4}T$, $_{6}^{5}T$ and $_{7}^{6}T$ represent the HTM of coordinate system 1/2/3/4/5/6/7 relative to coordinate system 0/1/2/3/4/5/6, respectively. To obtain the desired joint angle, the inverse kinematics analysis on the robot is performed. The inspection robot has seven joints and many variables, which are difficult to solve. The special structure of the inspection robot allows it to obtain the inverse kinematics expression without considering the last joint variable. At this time, the HTM of the global coordinate system at the end of the robot is shown in Eq. (6).

$$_{6}^{G}T = _{0}^{G}T \cdot _{1}^{0}T \cdot _{2}^{1}T \cdot _{3}^{2}T \cdot _{4}^{3}T \cdot _{5}^{4}T \cdot _{6}^{5}T = \begin{bmatrix} n_x' & o_x' & a_x' & p_x' \\ n_y' & o_y' & a_y' & p_y' \\ n_z' & o_z' & a_z' & p_z' \\ 0 & 0 & 0 & 1 \end{bmatrix} \quad (6)$$

When the rotation of the second robotic arm is not 0, the analytical expressions for the first six joint variables are shown in Eq. (7).

$$\begin{cases} \theta_1 = \arctan\left(d_2 \sin\theta_1 / d_2 \cos\theta_1\right) \\ d_2 = d_2 \cos\theta_1 / \cos\theta_1 \\ \theta_3 = (\theta_1 + \theta_3) - \theta_1 \end{cases} \quad (7)$$

In Eq. (7), θ_1 represents the rotational amount of the claw

1. d_2 represents the extension and retraction amount of arm 1. θ_3 represents the rotation amount of arm 1. When the rotation of the arm 2 is 0, the analytical expressions for the first six joint variables are shown in equation (8).

$$\begin{cases} \theta_1 = \arcsin o_x \\ d_2 = \dfrac{\dfrac{p_x - 266}{\sin\theta_1} + \left(\dfrac{p_z}{-\cos\theta_1}\right)}{2} \\ d_6 = \dfrac{\dfrac{p_x - 266}{\sin\theta_1} - \left(\dfrac{p_z}{-\cos\theta_1}\right)}{2} \end{cases} \quad (8)$$

In Eq. (8), d_6 represents the telescopic amount of arm 2. The length of each push rod is shown in Eq. (9).

$$\begin{cases} l_1 = \sqrt{s_2^2 + s_3^2 - 2 s_2 s_3 \cos\left(\dfrac{\pi}{2} - \alpha_1 + \alpha_3 - \theta_1\right)} \\ l_3 = \sqrt{s_4^2 + s_5^2 - 2 s_4 s_5 \cos\left(\pi - \beta_1 - \beta_2 + \theta_3\right)} \\ l_4 = \sqrt{s_6^2 + s_7^2 - 2 s_6 s_7 \cos\left(\pi - \gamma_1 - \gamma_2 + \theta_4\right)} \\ l_5 = \sqrt{s_4^2 + s_5^2 - 2 s_4 s_5 \cos\left(\pi - \beta_1 - \beta_2 + \theta_5\right)} \\ l_1 = \sqrt{s_2^2 + s_3^2 - 2 s_2 s_3 \cos\left(\dfrac{\pi}{2} - \alpha_1 + \alpha_3 - \theta_7\right)} \end{cases} \quad (9)$$

In Eq. (9), l_1-l_7 respectively represent the length of the push rod that adjusts the corresponding joint variable.

B. Obstacle Crossing Path Planning Algorithm for TLIR

To ensure the collision free motion of the TLIR during the operation, an obstacle crossing path planning algorithm based on the improved RRT-Connect algorithm is proposed by combining its kinematic analysis model. RRT is a path planning algorithm based on random sampling, which can effectively overcome the high dimensionality caused by motion. The search tree extension diagram of the RRT is displayed in Fig. 4.

In Fig. 4, when using the initial point as the extended root node and conducting search expansion in space, each search randomly generates sampling points. If the distance between the random sampling point and its nearest point is greater than the set extension step, the nearest point will be extended to the random sampling point at the set step size, generating a new node. Otherwise, the random sampling points are used as new nodes [15-17]. If the connection between the new node and the nearest node collides with an obstacle, the new node will be abandoned. Otherwise, the new node is added to the random tree. The distance between nodes is shown in Eq. (10).

$$\rho(x_1, x_2) = \|x_2 - x_1\| \quad (10)$$

In Eq. (10), x_1 and x_2 represent different nodes. The new node is shown in Eq. (11).

$$x_{new} = x_{near} + \lambda \frac{x_{rand} - x_{near}}{\|x_{rand} - x_{near}\|} \qquad (11)$$

In Eq. (11), x_{new} represents the new node. x_{near} represents the node closest to the random sampling point. x_{rand} represents a random sampling point. λ represents the extension step size. The RRT algorithm has strong randomness, resulting in a large number of redundant nodes. Path planning takes a long time. The RRT-Connect algorithm improves the search speed by incorporating the Connect heuristic algorithm on the basis of bidirectional RRT algorithm, which has a certain degree of directionality. The new node generation method of RRT-Connect algorithm is shown in Eq. (12).

$$\begin{cases} x_{new} = x_{near}(a + \varepsilon \cos\theta, b + \varepsilon \sin\theta) \\ \theta = \arctan(x_{t\arg et}(b) - x_{near}(b), x_{t\arg et}(a) - x_{near}(a)) \end{cases} \qquad (12)$$

In Eq. (12), (a,b) represents the node coordinates. θ represents the growth angle between the line connecting the target node and the nearest node and the horizontal line. ε represents the minimum fixed step size. $x_{t\arg et}$ represents the target node. The RRT-Connect greatly improves the efficiency of path planning. However, the mapping relationship between the joint space and workspace of the TLIR is complex, resulting in significant differences in the pose changes between the new

node and the parent node in the workspace. It is difficult to apply to the obstacle crossing path planning. Therefore, the RRT-Connect algorithm is improved by improving joint motion, search step size, and setting intermediate random trees. During robot collision detection, when there is a significant change in the end pose of the workspace between two nodes, interpolation collision detection needs to be performed between the two nodes. At this point, it is difficult to distinguish the impact of different joint movements on the changes in workspace posture. Therefore, to simplify the collision detection process, a path search method based on single joint motion is proposed, which means that the child nodes only change one joint during the expansion process [18-20]. Although the single joint motion path search method can achieve clear correspondence between joint space and workspace pose. However, in joint space, different single joint movements can still cause changes in the workspace posture. Therefore, to simplify the search process, the fixed position step size is set within the workspace instead of the joint space. At this point, collision detection only needs to detect the sampling points and nearest nodes, which greatly reduces the workload of joint space collision detection. In addition, the RRT-Connect algorithm is prone to getting stuck in local search when encountering large obstacles. A large number of random sampling points from other directions need to be generated to cross the obstacle. Therefore, to alleviate the local search problem, a random tree with an intermediate point is set in the middle of the path. The improved RRT-Connect path planning process is displayed in Fig. 5.
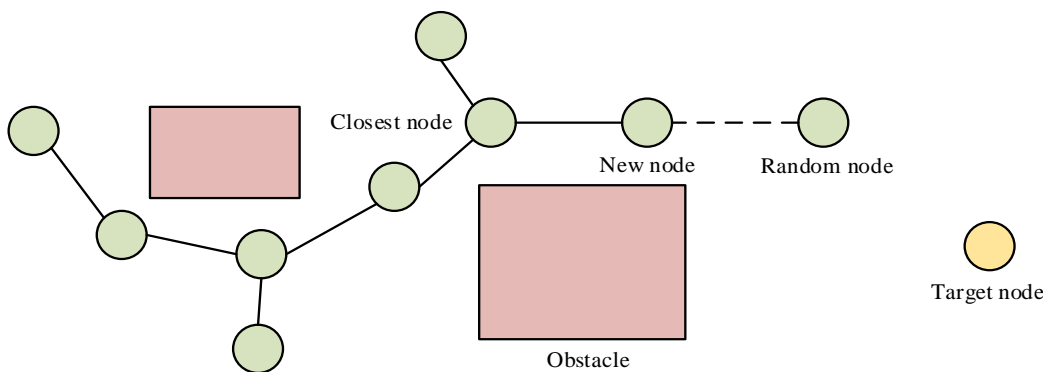

Fig. 4.   Search tree extension plot of the RRT algorithm.
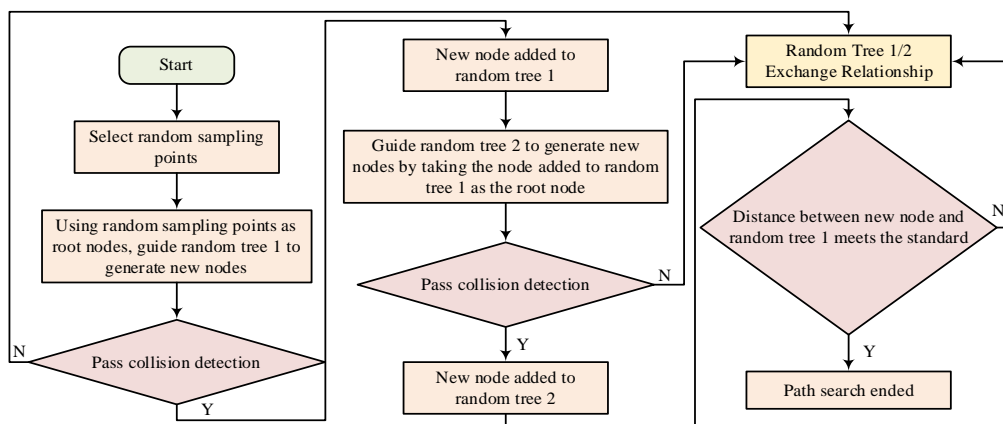

Fig. 5.   The RRT-Connect path planning process.

From Fig. 5, firstly, a random sampling point is selected and used as the root node to guide random tree 1. A new node is generated. If the new node has not collided, it will be added to random tree 1. Otherwise, the node will be abandoned. After adding a new node to random tree 1, guide random tree 2 to generate a new node with that node as the root node. If the new node passes collision detection, it will be added to random tree 2. Otherwise, abandon the new node. After adding a new node to random tree 2, if the distance between the node and random tree 1 meets the standard, complete the path search. Otherwise, the relationship between the two random trees will be swapped. The improved RRT-Connect algorithm can obtain discrete path nodes. However, in the actual motion of the inspection robot, the trajectory of the push rod length needs to be planned to control the motion of the inspection robot. The trajectory of the push rod planned by the quintic polynomial interpolation method is shown in Eq. (13).

$$d(t) = m_0 + m_1 t + m_2 t^2 + m_3 t^3 + m_4 t^4 + m_5 t^5 \qquad (13)$$

In Eq. (13), t represents the movement time of the push rod. m_0 - m_5 represent polynomial coefficients. The initial time is 0. The boundary condition is displayed in Eq. (14).

$$\begin{cases} d_1 = m_0 \\ v_1 = m_1 \\ a_1 = 2m_2 \\ d_2 = m_0 + m_1 t_2 + m_2 t_2^2 + m_3 t_2^3 + m_4 t_2^4 + m_5 t_2^5 \\ v_2 = m_1 + 2m_2 t_2 + 3m_3 t_2^2 + 4m_4 t_2^3 + 5m_5 t_2^4 \\ a_2 = 2m_2 + 6m_3 t_2 + 12m_4 t_2^2 + 20m_5 t_2^3 \end{cases} \qquad (14)$$

In Eq. (14), d_1 and d_2 represent the initial length and termination length of the push rod, respectively. v_1 and v_2 represent the initial speed and end speed of the push rod. a_1

and a_2 are the initial acceleration and termination acceleration, respectively. t_1 and t_2 represent the initial and ending times, respectively. The coefficients of the five term equation can be obtained from the above equation, as shown in Eq. (15).

$$\begin{cases} m_0 = d_1 \\ m_1 = v_1 \\ m_2 = \dfrac{a_1}{2} \\ m_3 = \dfrac{20(d_2 - d_1) - (12v_1 + 8v_2)t_2 - (3a_1 - a_2)t_2^2}{2t_2^3} \\ m_4 = \dfrac{-30(d_2 - d_1) + (16v_1 + 14v_2)t_2 + (3a_1 - 2a_2)t_2^2}{2t_2^4} \\ m_5 = \dfrac{12(d_2 - d_1) - (6v_1 + 6v_2)t_2 - (a_1 - a_2)t_2^2}{2t_2^5} \end{cases} \qquad (15)$$

Based on the quintic polynomial interpolation method, the speed, length, motion speed, and acceleration of the push rod are controlled, thereby achieving motion control of the inspection robot.

IV. SIMULATION ANALYSIS OF OBSTACLE CROSSING PERFORMANCE FOR TLIR

To test the obstacle crossing ability of the TLIR, simulation testing was performed. The obstacles selected in the experiment were the vibration damper and suspension clamp and insulator string. The lengths of the enclosure box for the vibration damper, suspension clamp, and insulator string were 50mm, 160mm, and 1150mm, respectively. The radii were 35mm, 45mm, and 100mm, respectively. The step size of the workspace was 30mm. The joint configurations of random tree root nodes for different obstacles were shown in Table I.

TABLE I.   JOINT CONFIGURATIONS OF RANDOM ROOT NODES FOR DIFFERENT OBSTACLES

Node	θ1/rad	d2/mm	θ3/rad	θ4/rad	θ5/rad	d6/mm	θ7/rad
Starting point of vibration damper	0.24	494.3	-0.24	0	-0.24	494.3	3.38
Midpoint of vibration damper	0.61	550.1	-0.61	0.44	-0.61	550.1	3.23
End of vibration damper	1.05	660.1	-1.05	0	-1.05	660.1	4.19
Starting point of insulator string	0.24	494.3	-0.24	0	-0.24	494.3	3.38
Midpoint of insulator string	0.56	586.0	-0.75	0.79	-0.56	577.0	2.71
End of insulator string	0.79	660.4	-0.79	0	-0.79	660.4	3.93

From Table I, when the inspection robot crossing different obstacles, the root node joint configuration of its random tree was different. When crossing the suspension clamp and insulator string, the output curve of the inspection robot is shown in Fig. 6.

In Fig. 6(a), when the crossing the suspension clamp and insulator string, the angle output range of claw 1 and arm 1 was (50°~120°) and (50°, 80°). The angle output ranges of the claw 2, bracket 2, and arm 2 were (20°, 90°), (0°, 60°), and (-60°, 0°).

From Fig. 6(b), during the obstacle crossing process, the length output range of the push rods in numbers 1 and 2 was (468585)mm. According to Fig. 6, the end trajectory in the rear arm obstacle crossing is based on the front claw center as the reference point for the end base coordinate, and its path is the same as the front claw obstacle crossing trajectory. This proves that the symmetrical structure of the robot can simplify the obstacle crossing process by making the process of crossing obstacles with the backward paw the reverse movement of the front paw when crossing simple obstacles. The displacement of

each joint and push rod when the inspection robot crossed the suspension clamp and insulator string is shown in Fig. 7.

In Fig. 7(a), when crossing the suspension clamp and insulator string, the rotation ranges of claw 1 and arm 1 were (-50°~20°) and (-20°, 10°). The rotation ranges of claw 2, bracket 2, and arm 2 were (-20°, 50°), (0°, 60°), and (-10°, 20°). From Fig. 7(b), during the obstacle crossing process, the extension range of push rods 1 and 2 was (0, 125) mm. The extension range of the middle push rods 1 and 2 was (-15, 115) mm. The extension range of the lower push rods 1 and 2 was (-25, 0) mm. The extension range of the horizontal push rods 1 and 2 was (0, 30) mm. From Fig. 7, the motion process of the front claw under the reference mark when crossing obstacles is opposite to that of the rear claw when crossing obstacles under the reference mark. If the starting point of the obstacle crossing at a distance of 500mm from the hanging clamp on the wire is taken as the base coordinate, the simplified model of the rotation joint rotation angle and push rod displacement change process in the front claw obstacle crossing is mirrored to the rotation joint rotation angle and push rod displacement change process in the

rear claw motion. From this, the robot's obstacle crossing movement is relatively stable. The output speed of each joint and push rod of the inspection robot is shown in Fig. 8.

From Fig. 8(a), when crossing the suspension clamp and insulator string, the rotational speeds of the claw 1 and arm 1 were (-7.5~7.5) deg/s and (-1.5, 1.5) deg/s. The rotational speeds of the claw 2, bracket 2, and arm 2 were (-7.5~7.5) deg/s, (-4, 11.5) deg/s, and (-1.5, 1.5) deg/s. From Fig. 8(b), during the obstacle crossing process, the telescopic speeds of push rods 1 and 2 were both (-13, 10) mm/s. The extension speeds of push rods 1 and 2 were both (-7.5, 8.5) mm/s. The telescopic speeds of the lower push rods 1 and 2 were both (-2.5, 2.5) mm/s. The telescopic speed of the horizontal push rods 1 and 2 was (-2.5, 6) mm/s. The speed change curve of each joint and push rod of the inspection robot was smooth, indicating that the acceleration value was not large. The motion of the inspection robot was relatively stable. When climbing over the shock absorber, the output curve of the inspection robot is shown in Fig. 9.
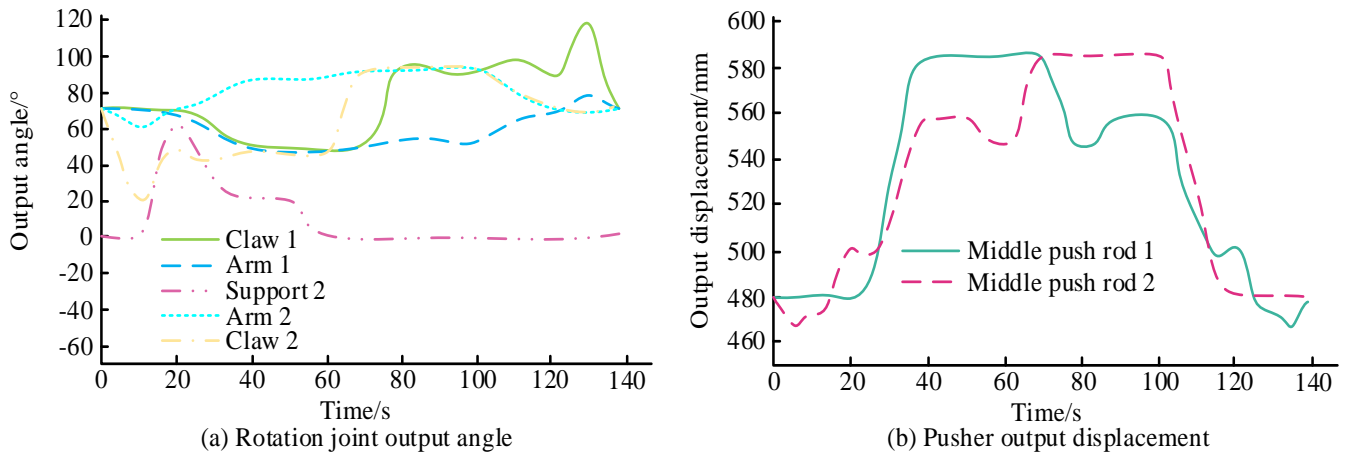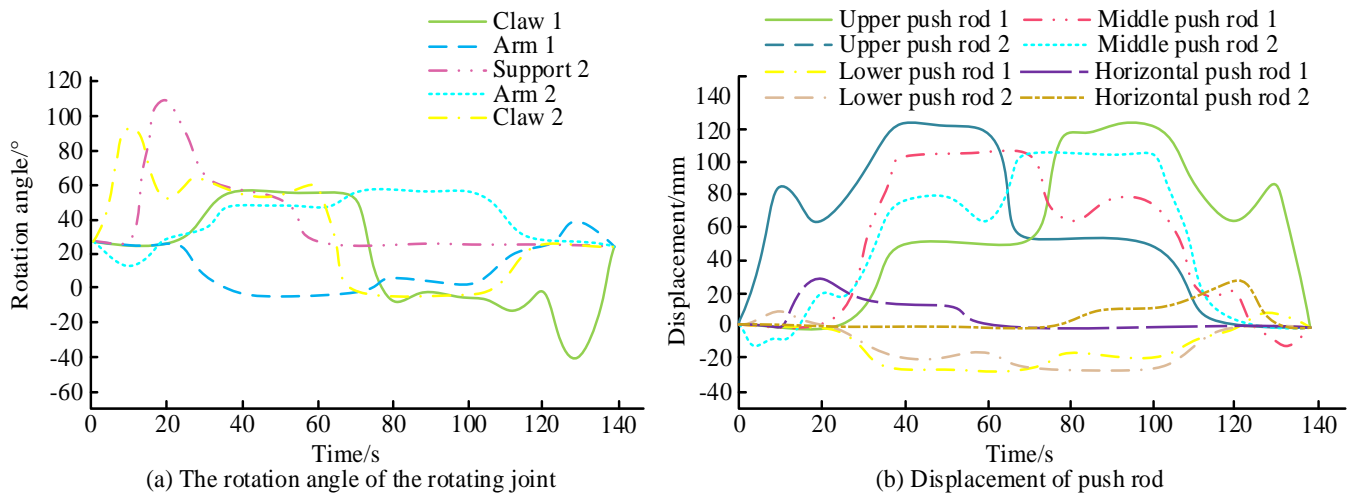

(a) Rotation joint output angle

(b) Pusher output displacement

Fig. 6.   Output curve of the inspection robot.

(a) The rotation angle of the rotating joint

(b) Displacement of push rod

Fig. 7.   Displacement of the joints and push rods of the inspection robot.

(a) The rotational speed of the rotating joint

(b) The speed of the push rod

Fig. 8. Output speed of each joint and push rod of the inspection robot.

(a) Rotation joint output angle

(b) Pusher output displacement

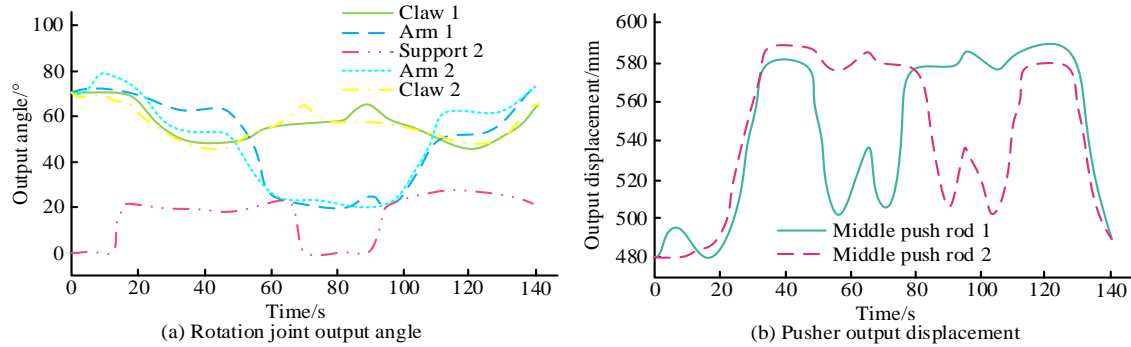Fig. 9. Output curve of the inspection robot.

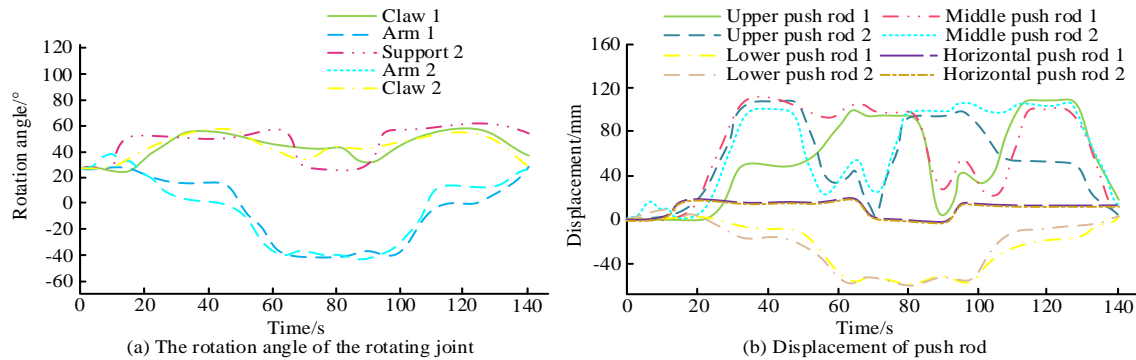(a) The rotation angle of the rotating joint
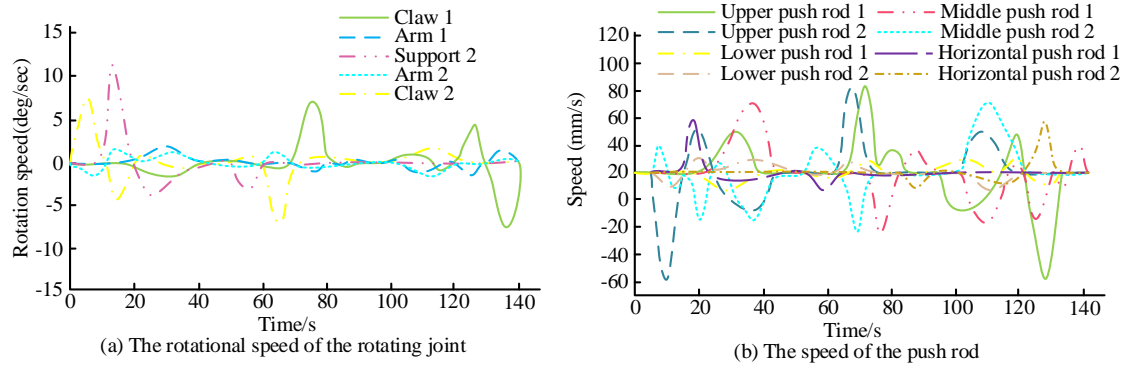
(b) Displacement of push rod

Fig. 10. Displacement of the joints and push rods of the inspection robot.

In Fig. 9(a), when overtaking the vibration damper, the angle output ranges of claw 1 and arm 1 were (50°~70°) and (20°, 80°). The angle output ranges of the claw 2, bracket 2, and arm 2 were (45°, 70°), (0°, 25°), and (0°, 25°). From Fig. 9(b), during the obstacle crossing process, the length output range of push rods 1 and 2 was (480, 590) mm. From Fig. 9, the obstacle crossing trajectory of the robot's front and rear claws over the shock absorber is basically consistent with the planned end trajectory. In order to save time, the trajectory of the rear claw passing through the end of the shock absorber does not need to be completely mirrored with the front claw, which can make it closer to the turning point of the planned path. When climbing over the vibration damper, the displacement of each joint and push rod is shown in Fig. 10.

From Fig. 10(a), the rotation ranges of claw 1 and arm 1 were (0°~22°) and (-50°, 10°) when overtaking the vibration hammer. The rotation ranges of the bracket 2, arm 2, and claw

2 were (0°, 25°), (-50°, 10°), and (0°, 22°). From Fig. 10(b), during the obstacle crossing process, the extension range of push rods 1 and 2 was (0, 100) mm. The extension range of the push rods 1 and 2 was (0, 110) mm. The extension ranges of the lower push rods 1 and 2 were (-60, 10) mm. The extension ranges of the horizontal push rods 1 and 2 were (0, 20) mm. When climbing over the vibration hammer, the output speed of each joint and push rod of the inspection robot is shown in Fig. 11.

From Fig. 11(a), the rotational speeds of the claw 1 and the arm 1 were (-1.5~1.5) deg/s and (-3, 2.5) deg/s when overtaking the damper. The rotational speeds of the bracket 2, arm 2, and claw 2 were (-3.5~3.5) deg/s, (-2.5, 3) deg/s, and (-27, 2) deg/s. From Fig. 11(b), during the obstacle crossing process, the extension speeds of push rods 1 and 2 were (-17, 13.5) mm/s and (-13.5, 17) mm/s, respectively. The extension ranges of push rods 1 and 2 were (-11, 11) mm/s. The extension speeds of

the lower push rods 1 and 2 were (-4.5, 3) mm/s and (-3, 4.5) mm/s, respectively. The stretching and retracting speeds of the horizontal push rods 1 and 2 were all (-4, 5) mm/s. When the inspection robot climbed over the vibration hammer, the speed

change curve of each joint and push rod was smooth. It indicated that the motion of the inspection robot was relatively stable.
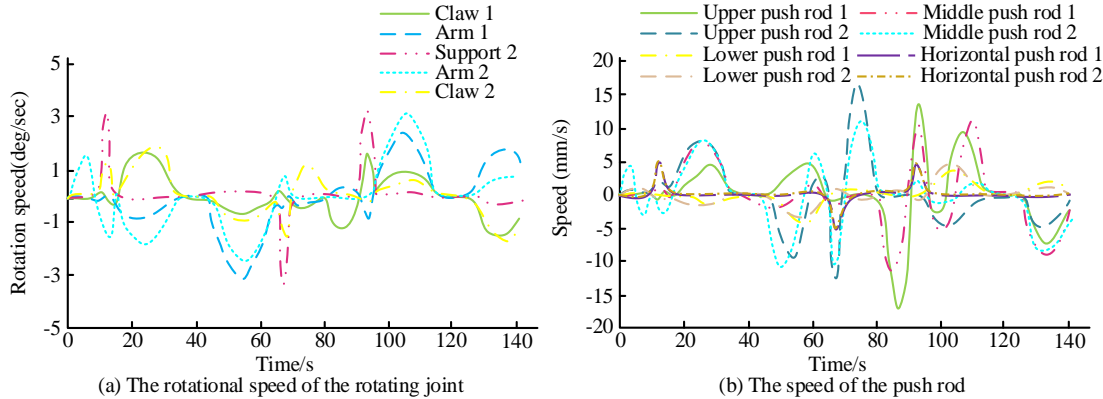

Fig. 11. Output speed of each joint and push rod of the inspection robot.

V. DISCUSSION

As an indispensable part of social production activities and people's lives, electricity plays an irreplaceable role in the development of the national economy. Overhead transmission lines are the hub responsible for transportation in the entire power system. It is necessary to conduct regular inspections and maintenance of high-voltage overhead transmission lines that are exposed to harsh natural environments all year round to ensure the safe and stable operation of the power transportation network. Compared with manual inspection, helicopter inspection, and drone inspection, online inspection robots have advantages such as low cost, high quality, and long operating time. To this end, the study conducted kinematic analysis on the inspection robot to understand its motion patterns during obstacle crossing. An obstacle crossing path planning algorithm based on an improved RRT-Connect algorithm was proposed. The experimental results showed that when the inspection robot crossed the insulator string of the suspension clamp, the angle output ranges of the first claw and the first arm were (50°~120°) and (50°, 80°). The angle output ranges of claw 2, bracket 2, and arm 2 were (20°, 90°), (0°, 60°), and (-60°, 0°). The corresponding rotational speeds were (-7.5~7.5) deg/s, (-1.5, 1.5) deg/s, (-7.5~7.5) deg/s, (-4, 11.5) deg/s, and (-1.5, 1.5) deg/s. The extension and contraction ranges of the upper/middle/lower/horizontal push rods were (0125) mm, (-15, 115) mm, (-25, 0) mm, and (0, 30) mm, respectively, with corresponding extension and contraction speeds of (-13, 10) mm/s, (-7.5, 8.5) mm/s, (-2.5, 2.5) mm/s, and (-2.5, 6) mm/s. According to the experimental results, the proposed inspection robot has stable changes in the angle (displacement) and velocity curves of its joints and push rods when crossing obstacles, without any abrupt changes. The same conclusion can also be observed from the graph of velocity and acceleration. At the same time, the velocity curves of push rods in each joint of the robot are smooth, and the acceleration values are not large. Therefore, the robot's obstacle crossing motion is relatively stable and has good kinematic performance. In addition, the output changes of each push rod obtained in the end path planning of the line patrol robot can enable the robot to complete the planned action along the predetermined

trajectory at the obstacle crossing end.

VI. CONCLUSION

As the key to power transmission, transmission lines need to be regularly inspected to ensure safety and stability. The inspection robot has low cost and long running time in the inspection of transmission lines. It can promptly troubleshoot faults on transmission lines. To ensure that the inspection robot can achieve collision free motion in the inspection project, the kinematic analysis is conducted on the inspection robot to analyze the motion laws during obstacle crossing. An obstacle crossing path planning algorithm based on the improved RRT-Connect algorithm is proposed. In order to verify the effectiveness of the obstacle crossing method proposed in the study, simulations were conducted based on the obstacle crossing path of the robot's end effector. Real-time rotation angles, output displacement, and velocity curves of each joint and push rod during different obstacle crossing processes were obtained. Kinematic equations were used to further represent the variation curves of each joint. The output changes of each push rod obtained in the end path planning of the line inspection robot can enable the robot to complete the planned action along the predetermined trajectory at the obstacle crossing end, and ensure the stability of the inspection robot during obstacle crossing. Although the obstacle crossing method proposed in the study can effectively ensure the motion stability of the inspection robot, there are still many redundant trajectories in its workspace. Therefore, future work will focus on how to eliminate redundant trajectories.

REFERENCES

[1] Luo X J, Zhang LL. Adaptive Morphological Filter for Extracting Features of Fault on Transmission Line. IEEJ Transactions on Electrical and Electronic Engineering, 2022, 17(9):1364-1366.

[2] Viswavandya M, Patel S, Sahoo K. Analysis and Comparison of Machine Learning Approaches for Transmission Line Fault Prediction in Power Systems. Journal of Research in Engineering and Applied Sciences, 2021, 6(1):24-31.

[3] Nie Y, Liu Y, Lu D, & Wang B. An improved natural frequency based transmission line fault location method with full utilization of frequency spectrum information. IET Generation, Transmission & Distribution, 2021, 15(19):2787-2803.

[4] Hernando M, Brunete A, Gambao E. ROMERIN: A Modular Climber Robot for Infrastructure Inspection. IFAC-PapersOnLine, 2019, 52(15):424-429.

[5] Wang Y, Yuan C, Zhai Y. Mechanism Design and Analysis of a New Overhead Transmission Line Inspection Robot. Journal of Northwestern Polytechnical University, 2020, 38(5):1105-1111.

[6] Wei J, Hua Z D, Shuangbao M, Gaocheng Y, & Wei C. Dynamic walking characteristics and control of four-wheel mobile robot on ultra-high voltage multi-split transmission line. Transactions of the Institute of Measurement and Control, 2022, 44(6):1309-1322.

[7] Huang X, Wu Y, Zhang Y, & Zhang H. A Method of Transmission Conductor Loosened Detect Based on Image Sensors. IEEE Transactions on Instrumentation and Measurement, 2020,69P(11):8783-8796.

[8] Qingkai Z, Qingwu L, Chang X, Qiuyu L, & Yaqin Z. Class-aware edge-assisted lightweight semantic segmentation network for power transmission line inspection. Applied Intelligence: The International Journal of Artificial Intelligence, Neural Networks, and Complex Problem-Solving Technologies, 2023, 53(6):6826-6843.

[9] Xiong S, Liu Y, Yan Y, Pei L, Xu P, & Fu X, et al. Object recognition for power equipment via human level concept learning. IET Generation, Transmission & Distribution, 2021, 15(10):1578-1587.

[10] Hu B, Cao Z, Zhou M. An Efficient RRT-based Framework for Planning Short and Smooth Wheeled Robot Motion under Kinodynamic Constraints. IEEE Transactions on Industrial Electronics, 2020, 68(4):3292-3302.

[11] Sun Y, Zhang C, Sun P, & Liu C. Safe and Smooth Motion Planning for Mecanum Wheeled Robot Using Improved RRT and Cubic Spline. Arabian Journal for Science and Engineering. Section A, Sciences, 2020, 45(4):3075-3090.

[12] Jhang J H, Lian F L, Hao Y H. Human-like motion planning for autonomous parking based on revised bidirectional rapidly-exploring random tree with Reeds-Shepp curve. Asian Journal of Control, 2021, 23(3):1146-1160.

[13] Zammit C, Kampen E J V. Real-time 3D UAV Path Planning in Dynamic Environments with Uncertainty. Unmanned Systems, 2023, 11(3):203-219.

[14] Wang J, Hirota K, Wu X,Dai Y, & Jia Z. Hybrid Bidirectional Rapidly Exploring Random Tree Path Planning Algorithm with Reinforcement Learning. Journal of Advanced Computatioanl Intelligence and Intelligent Informatics, 2021, 25(148):121-129.

[15] Choudhuri S, Adeniye S, Sen A. Distribution Alignment Using Complement Entropy Objective and Adaptive Consensus-Based Label Refinement for Partial Domain Adaptation, Artificial Intelligence and Applications. 2023, 1(1): 43-51.

[16] Belaid A, Mendil B, Djenadi A. Narrow passage RRT*: a new variant of RRT*. International journal of computational vision and robotics, 2022, 12(1):85-100.

[17] Huang G, Ma Q. Research on Path Planning Algorithm of Autonomous Vehicles Based on Improved RRT Algorithm. International journal of intelligent transportation systems research, 2022, 20(1):170-180.

[18] Wang X, Xia Z, Zhou X, Wei J, Gu X, & Yan H. Collision-Free Path Planning for Arc Welding Robot Based on Ida-De Algorithm. International Journal of Robotics & Automation, 2022, 37(6):476-485.

[19] Babel L. Online flight path planning with flight time constraints for fixed-wing UAVs in dynamic environments. International journal of intelligent unmanned systems, 2022, 10(4):130-157.

[20] Christensen R S, Droge G, Leishman R C. Closed-Loop Linear Covariance Framework for Path Planning in Static Uncertain Obstacle Fields. Journal of Guidance, Control, and Dynamics: A Publication of the American Institute of Aeronautics and Astronautics Devoted to the Technology of Dynamics and Control, 2022, 45(4):669-683.